Impedance Characteristic Analysis and Oscillation Suppression for Wind Power Integrated System Based on Uncertainty and Disturbance Estimator

Yanhui Xu and Jiayan Li

***Abstract*—Under weak grid conditions, oscillation in wind power integrated system occurs frequently. However, existing oscillation suppression methods face challenges in effectively coordinating control parameters and fail to guarantee excellent dynamic performance. Therefore, this paper proposes an uncertainty and disturbance estimator-based feedback linearization sliding mode control (UDE-FLSMC) method, which can reduce the negative damping region of the impedance phase of wind power integrated system. Firstly, the feedback linearization process of multi-input multi-output (MIMO) systems is derived. Then, the uncertainty and disturbance estimator (UDE) is used to estimate the disturbance in sliding mode control, and the UDE-FLSMC method is proposed. Secondly, the control structure and impedance model of wind power grid-side converter (GSC) are established. The impact of control parameters on the impedance characteristics of the converter is analyzed. It is demonstrated that the impedance phase in sub/supersynchronous frequency band maintains within a significant positive damping region under different operating conditions. Then, a hardware-in-loop experimental platform is constructed to verify the dynamic performance of the proposed UDE-FLSMC method, which is compared with proportional integral (PI) control and phase margin frequency division compensation (PM-FDC) control. The results show that the proposed UDE-FLSMC method exhibits superior oscillation suppression ability and faster response characteristics, which can significantly improve the stability of wind power integrated system under weak grid conditions.**

***Index Terms*—Oscillation suppression, impedance, uncertainty, disturbance, converter, sliding mode control, wind power integrated system, weak grid.**

I. Introduction

To address the increasingly severe energy crisis and climate challenges, renewable energy sources represented by wind turbines and photovoltaics have experienced rapid development. The current power system is undergoing a critical period of transition from traditional systems dominated by synchronous generators to new-type power systems dominated by renewable energy sources [1]-[3]. However, the integration of a large number of power electronic devices reduces the power system inertia and damping, resulting in wideband oscillation events that occur frequently, which severely impacts the stable operation of power system. For example, in 2012, a sub-synchronous oscillation (SSO) event caused by interaction between doubly-fed induction generators (DFIGs) and series-compensated capacitors occurred in the Guyuan area of North China, resulting in the disconnection of a large number of wind turbines [4]. In 2015, a sub-/super-synchronous oscillation event triggered by the interaction between direct-drive permanent magnet synchronous generators (PMSGs) and a weak grid occurred in the Hami area of Xinjiang, China. The oscillation signals propagated to steam turbine units 300 km away, inducing shaft torsional vibrations and subsequent tripping [5].

To enhance the stability of renewable energy integrated systems and mitigate the risks posed by wideband oscillations, researchers have conducted studies on oscillation suppression methods from three perspectives: parameter optimization, impedance reshaping, and robust control. By designing and optimizing the control loop parameters for power electronic devices, the damping level and stable operational capability of the equipment can be effectively enhanced. References [6] and [7] have shown that the phase-locked loop (PLL) bandwidth determines the negative damping region in the low-frequency band, and the negative damping reaches its maximum when the PLL bandwidth is close to the voltage loop bandwidth [8]. However, reducing the PLL bandwidth can narrow this negative damping region, which may degrade the dynamic response speed of power system [9]. Reference [10] establishes the correlation between PLL parameters and stability margin, then proposes a parameter optimization design method based on the damping ratio and natural frequency. Reference [11] considers the frequency coupling effect when grid impedance varies, and then proposes an optimization design method for voltage loop control

Manuscript received: March 4, 2025; revised: April 27, 2025; accepted: June 19, 2025. Date of CrossCheck: June 19, 2025. Date of online publication: July 3, 2025.

This work was supported by the National Natural Science Foundation of China (No. 52377102).

Y. Xu (corresponding author) and J. Li are with the State Key Laboratory of Alternate Electrical Power System with Renewable Energy Sources, North China Electric Power University, Beijing 102206, China (e-mail: xuyanhui23@sohu.com; lijiayan@ncepu.edu.cn).

DOI: 10.35833/MPCE.2025.000175

parameters. Reference [12], focusing on wind power integrated systems via voltage source converter based high-voltage direct current (VSC-HVDC), reveals that increasing the proportional coefficient of the voltage loop in VSC-HVDC can enhance the phase margin and improve the system stability. Reference [13] modifies the high-frequency impedance characteristics of HVDC system by optimizing the current loop parameters, avoiding high-frequency impedance resonance points. However, due to the large number of control parameters, it is difficult to coordinate the parameters in different control links, and it needs to be re-optimized at different power levels.

Impedance characteristic analysis can visualize the oscillation risks in different frequency bands of renewable energy integrated systems. Impedance reshaping for specific frequency bands is effective for oscillation suppression [14]. Reference [15] proposes an impedance reshaping strategy that combines active damping and virtual admittance, optimizing the impedance characteristics in the current loop frequency band and the medium-to-high-frequency band, thereby reducing the risk of oscillations across the entire frequency range. Reference [16] introduces a phase margin frequency division compensation (PM-FDC) method, which offsets the negative damping effect of the PLL in the low-frequency band through a compensation matrix and achieves phase compensation for negative damping outside the current loop bandwidth via lead correction. Reference [17] proposes an impedance reshaping strategy based on grid voltage feedforward, which utilizes function approximation and multi-objective constraints to design the grid voltage feed-forward function, broadening the adaptive range to the grid impedance. Reference [18] proposes a virtual series-based impedance reshaping method, which does not require grid impedance estimation and is robust against system parameter variations. Based on that, the inverter system can operate stably even under very weak grid conditions. Reference [19] proposes an enhanced impedance reshaping control, which can effectively mitigate the frequency coupling of the medium-to-high-frequency band impedance, and improve the negative damping characteristics. Configuring grid-forming units in a reasonable proportion at renewable energy stations can also improve the impedance characteristics [20]. However, impedance reshaping based oscillation suppression methods may affect the dynamic performance of the power system [21].

Optimizing and improving the control structure of renewable energy devices based on robust control could achieve a better oscillation suppression effect without affecting the dynamic performance. Reference [22] designs a nonlinear damping controller using partial feedback linearization aimed at mitigating sub-synchronous resonance problem of DFIG-based wind farms via series compensation. Reference [23] proposes a sliding mode variable structure control based on feedback linearization, which is used in the rotor-side converter control loop of DFIG to suppress the sub-synchronous control interactions. Reference [24] proposes a composite control that combines the fixed-time sliding mode disturbance observer with continuous finite-time backstepping control. The converter exhibits satisfactory tracking performance, robustness, and immunity ability in the face of various uncertainties. References [25] and [26] propose a sub-synchronous oscillation suppression method based on the feedback linearization theory and sliding mode control for PMSG-based wind farms connected to the power system via HVDC, taking into account the nonlinearity and uncertainty of the system. The uncertainty and disturbance estimator (UDE) is a robust control method that estimates uncertainties and disturbances within a certain range through low-pass filter. It can effectively address issues arising from parameter uncertainties and external disturbances in the system [27]. Reference [28] introduces an additional damping branch based on the UDE into the current loop of grid-forming wind turbines, which can reduce the negative damping region in the impedance phase and effectively suppress sub-synchronous oscillations. Reference [29] proposes a two-degree-freedom control algorithm based on the UDE, which introduces a delay effect in the low-pass UDE filter to enhance the suppression effect of harmonics from typical nonlinear loads.

In real engineering applications, the grid operation mode is complex and variable, and the short-circuit ratio (SCR) varies within a wide range. Therefore, the parameter optimization based method is difficult to adapt different operating conditions, while the impedance reshaping based method is difficult to ensure the dynamic performance during normal operation. Therefore, the robust control based oscillation suppression methods hold greater research value.

This paper proposes an uncertainty and disturbance estimator-based feedback linearization sliding mode control (UDE-FLSMC) method, which can effectively suppress sub-/super-synchronous oscillation problem of wind power integrated system. The main contributions of this paper are summarized as follows.

1) UDE is used to estimate the disturbance in sliding mode control, which not only eliminates the chattering problem of the sliding surface, but also suppresses both matched and unmatched disturbances. Therefore, it is highly robust to uncertainties in the system.

2) Based on the proposed UDE-FLSMC method, the control structure of the wind power grid-side converter (GSC) is designed. Impedance characteristic analysis shows that the proposed UDE-FLSMC method can significantly enhance the positive damping region of the impedance phase and can be adapted to stable operation under various operating conditions.

3) A hardware-in-loop experimental platform based on Real-time Digital Simulator (RTDS) and Compact RIO (C-RIO) is constructed, and the dynamic performance and oscillation suppression effect of the proposed UDE-FLSMC method are tested in terms of oscillation suppression and anti-disturbance ability.

The remainder of this paper is organized as follows. Section II proposes the UDE-FLSMC method. Section III presents the application of the proposed UDE-FLSMC method in wind power integrated system. Section IV analyzes the impedance characteristics and stability of wind power integrated system. Section V presents the hardware-in-loop experimental verification. Section VI conclude this paper.

II. Proposed UDE-FLSMC Method

In this section, the system nonlinear term is eliminated based on feedback linearization. When there is a disturbance coupling between the internal and external system states, in order to further deal with the influence of the uncertain disturbances on system stability, the UDE-FLSMC method is proposed, which can effectively suppress the sub-/super-synchronous oscillation problem induced by the system disturbances.

A. Feedback Linearization of Multi-input Multi-output (MIMO) Systems with Disturbance

Consider a nonlinear system with bounded disturbance as:

$$\begin{cases} \dot{\boldsymbol{x}}=\boldsymbol{f}(\boldsymbol{x})+\Delta\boldsymbol{f}(\boldsymbol{x})+\big(\boldsymbol{g}(\boldsymbol{x})+\Delta\boldsymbol{g}(\boldsymbol{x})\big)\boldsymbol{u}+\boldsymbol{d}(\boldsymbol{x})\boldsymbol{w} \\ \boldsymbol{y}=\boldsymbol{h}(\boldsymbol{x}) \end{cases} \tag{1}$$

where $\boldsymbol{x}\in\mathbb{R}^n$ is the state vector; $\boldsymbol{u}\in\mathbb{R}^n$ is the control vector, $\boldsymbol{y}\in\mathbb{R}^n$ is the output vector; $\boldsymbol{f}(\boldsymbol{x})$ and $\boldsymbol{g}(\boldsymbol{x})$ are the n-dimensional smooth vector fields in the state space; $\boldsymbol{h}(\boldsymbol{x})$ is the scalar function of $\boldsymbol{x}$; $\Delta\boldsymbol{f}(\boldsymbol{x})$ and $\Delta\boldsymbol{g}(\boldsymbol{x})$ are the uncertain terms in the system model; $\boldsymbol{w}$ is an unexpected input or disturbance; and $\boldsymbol{d}(\boldsymbol{x})$ is a vector associated with the disturbance. Equation (1) can be transformed as:

$$\begin{cases} \dot{\boldsymbol{x}}=\boldsymbol{f}(\boldsymbol{x})+\boldsymbol{g}(\boldsymbol{x})\boldsymbol{u}+\boldsymbol{p}(\boldsymbol{x})\boldsymbol{w} \\ \boldsymbol{y}=\boldsymbol{h}(\boldsymbol{x}) \end{cases} \tag{2}$$

where $\boldsymbol{p}(\boldsymbol{x})\boldsymbol{w}=\Delta\boldsymbol{f}(\boldsymbol{x})+\Delta\boldsymbol{g}(\boldsymbol{x})\boldsymbol{u}+\boldsymbol{d}(\boldsymbol{x})\boldsymbol{w}$ is the lumped disturbance including system disturbance and uncertainty.

1) System Relative Degree

Each output $y_i=h_i(\boldsymbol{x})$ of an MIMO system has a sub-relative degree r_i, whose relative degree is a set denoted by $r=\{r_1, r_2, \ldots, r_m\}$. Each sub-relative degree must satisfy the following two conditions.

1) The k^{th}-order Lie derivative of the output function $\boldsymbol{h}(\boldsymbol{x})$ with respect to the vector field $\boldsymbol{f}(\boldsymbol{x})$ with respect to the vector field $\boldsymbol{g}(\boldsymbol{x})$ in the neighborhood of equilibrium point $\boldsymbol{x}^0$ is zero, which is expressed as:

$$\begin{cases} L_{g_1}L_f^k h_i(\boldsymbol{x})=0 \\ L_{g_2}L_f^k h_i(\boldsymbol{x})=0 \\ \vdots \\ L_{g_k}L_f^k h_i(\boldsymbol{x})=0 \\ k<r_i-1 \end{cases} \tag{3}$$

where $L_f^k h_i(\boldsymbol{x})$ is the i^{th} element of $L_f^k\boldsymbol{h}(\boldsymbol{x})$, $L_f^k\boldsymbol{h}(\boldsymbol{x})$ is the k^{th}-order Lie derivative of the function $\boldsymbol{h}(\boldsymbol{x})$ along $\boldsymbol{f}(\boldsymbol{x})$; and $L_{g_i}L_f^k\boldsymbol{h}(\boldsymbol{x})$ is the element of the Lie derivative of $L_f^k\boldsymbol{h}(\boldsymbol{x})$ along $\boldsymbol{g}(\boldsymbol{x})$.

2) The matrix $\boldsymbol{B}$ is non-singular in the neighborhood of equilibrium point $\boldsymbol{x}^0$.

$$\boldsymbol{B}=\begin{bmatrix} L_{g_1}L_f^{r_1-1}h_1 & L_{g_2}L_f^{r_1-1}h_1 & \cdots & L_{g_m}L_f^{r_1-1}h_1 \\ L_{g_1}L_f^{r_2-1}h_2 & L_{g_2}L_f^{r_2-1}h_2 & \cdots & L_{g_m}L_f^{r_2-1}h_2 \\ \vdots & \vdots & & \vdots \\ L_{g_1}L_f^{r_m-1}h_m & L_{g_2}L_f^{r_m-1}h_m & \cdots & L_{g_m}L_f^{r_m-1}h_m \end{bmatrix} \tag{4}$$

When the relative degree is equal to the system dimension ($r=n$), the accurate linearization of the exact state feedback can be achieved; while for the more general case where the relative degree is smaller than the system dimension ($r<n$), only partial feedback linearization can be achieved. At this point, the system dynamics can be divided into internal dynamics and external dynamics. For the external dynamics, both stability and good dynamic quality are required; while for the internal dynamics, only stability is required.

2) Nonlinear Coordinate Transformation

When $r<n$, the coordinate transformation of the feedback linearization process is given as:

$$\boldsymbol{\Phi}(\boldsymbol{x})=\begin{bmatrix} \varphi_1(\boldsymbol{x}) \\ \varphi_2(\boldsymbol{x}) \\ \vdots \\ \varphi_r(\boldsymbol{x}) \\ \varphi_{r+1}(\boldsymbol{x}) \\ \vdots \\ \varphi_n(\boldsymbol{x}) \end{bmatrix}=\begin{bmatrix} z_1 \\ z_2 \\ \vdots \\ z_r \\ z_{r+1} \\ \vdots \\ z_n \end{bmatrix}=\begin{bmatrix} \boldsymbol{h}(\boldsymbol{x}) \\ L_f\boldsymbol{h}(\boldsymbol{x}) \\ \vdots \\ L_f^{r-1}\boldsymbol{h}(\boldsymbol{x}) \\ \varphi_{r+1}(\boldsymbol{x}) \\ \vdots \\ \varphi_n(\boldsymbol{x}) \end{bmatrix} \tag{5}$$

where $\varphi_i(\boldsymbol{x})$ is the element of $\boldsymbol{\Phi}(\boldsymbol{x})$, and we use z_i to represent $\varphi_i(\boldsymbol{x})$. The first r equations denote the external dynamic coordinate transformations, which can be obtained from the Lie derivatives of the outputs with respect to the states; and the last $n-r$ equations denote the internal dynamic coordinate transformations, which can be obtained by the zero-dynamic design method. The selected coordinate transformations need to satisfy that the Jacobian matrix $\boldsymbol{J}_{\boldsymbol{\Phi}}$ in (6) is non-singular.

$$\boldsymbol{J}_{\boldsymbol{\Phi}}=\left.\frac{\partial\boldsymbol{\Phi}(\boldsymbol{x})}{\partial\boldsymbol{x}}\right|_{\boldsymbol{x}=\boldsymbol{x}^0}=\begin{bmatrix} \dfrac{\partial\varphi_1}{\partial x_1} & \dfrac{\partial\varphi_1}{\partial x_2} & \cdots & \dfrac{\partial\varphi_1}{\partial x_n} \\ \dfrac{\partial\varphi_2}{\partial x_1} & \dfrac{\partial\varphi_2}{\partial x_2} & \cdots & \dfrac{\partial\varphi_2}{\partial x_n} \\ \vdots & \vdots & & \vdots \\ \dfrac{\partial\varphi_n}{\partial x_1} & \dfrac{\partial\varphi_n}{\partial x_2} & \cdots & \dfrac{\partial\varphi_n}{\partial x_n} \end{bmatrix} \tag{6}$$

where x_i is the element of state vector $\boldsymbol{x}$. The system model after coordinate transformation is given as:

$$\begin{cases} \dot{z}_1=z_2+L_pL_f^0\boldsymbol{h}(\boldsymbol{x})\boldsymbol{w} \\ \dot{z}_2=z_3+L_pL_f^1\boldsymbol{h}(\boldsymbol{x})\boldsymbol{w} \\ \vdots \\ \dot{z}_{r-1}=z_r+L_pL_f^{r-2}\boldsymbol{h}(\boldsymbol{x})\boldsymbol{w} \\ \dot{z}_r=L_f^r\boldsymbol{h}(\boldsymbol{x})+L_gL_f^{r-1}\boldsymbol{h}(\boldsymbol{x})\boldsymbol{u}+L_pL_f^{r-1}\boldsymbol{h}(\boldsymbol{x})\boldsymbol{w} \\ \dot{z}_{r+1}=L_f\varphi_{r+1}(\boldsymbol{x})+L_g\varphi_{r+1}(\boldsymbol{x})\boldsymbol{u}+L_p\varphi_{r+1}(\boldsymbol{x})\boldsymbol{w} \\ \vdots \\ \dot{z}_n=L_f\varphi_n(\boldsymbol{x})+L_g\varphi_n(\boldsymbol{x})\boldsymbol{u}+L_p\varphi_n(\boldsymbol{x})\boldsymbol{w} \end{cases} \tag{7}$$

where $L_pL_f^k\boldsymbol{h}(\boldsymbol{x})$ is the Lie derivative of $L_f^k\boldsymbol{h}(\boldsymbol{x})$ along the vector field $\boldsymbol{p}(\boldsymbol{x})$. After partial feedback linearization, the external dynamic model is linear, while the internal dynamic model may be nonlinear. The first r state quantities of external dynamics and the $n-r$ state quantities of internal dynam-

ics are denoted by z_{vo} and z_{vi} as:

$$\begin{cases} z_{vo} = [z_1, z_2, ..., z_r]^T \\ z_{vi} = [z_{r+1}, z_{r+2}, ..., z_n]^T \end{cases} \tag{8}$$

Further, let the r^{th} equation in (7) be:

$$\boldsymbol{v} = L_f^r \boldsymbol{h}(\boldsymbol{x}) + L_g L_f^{r-1} \boldsymbol{h}(\boldsymbol{x}) \boldsymbol{u} \tag{9}$$

Equation (7) can be written in the following compact form as:

$$\begin{cases} \dot{z}_{vo} = \boldsymbol{A}\boldsymbol{z} + \boldsymbol{B}\boldsymbol{v} + \boldsymbol{c}(z)\boldsymbol{w}_2(z) \\ \dot{z}_{vi} = \boldsymbol{q}(z) + \boldsymbol{k}(z)\boldsymbol{w}_1(z) \end{cases} \tag{10}$$

where $\boldsymbol{A}$ is the state matrix; $\boldsymbol{B}$ is the control matrix; $\boldsymbol{c}(z)$ is the vector associated with external disturbance; $\boldsymbol{q}(z)$ is the internal dynamic model; $\boldsymbol{k}(z)$ is the vector associated with internal disturbance; and $\boldsymbol{w}_1(z)$ and $\boldsymbol{w}_2(z)$ are the bounded lumped disturbances containing disturbances and uncertainties. The first term in (10) is the linearized external dynamics model, and the second term is the internal dynamics model, which is only required to be stable, and therefore, may be nonlinear.

3) Disturbance Decoupling Condition

It is usually desired that the system output is not affected by disturbances at any moment, and a control system with this property is called output decoupling from disturbance system. The condition of output decoupling from disturbance is that the Lie derivative of the function $L_f^i \boldsymbol{h}(\boldsymbol{x})$ with respect to the vector field $\boldsymbol{p}(\boldsymbol{x})$ is zero in the neighborhood of $\boldsymbol{x}^0$:

$$L_p L_f^i \boldsymbol{h}(\boldsymbol{x}) = 0 \quad 0 \le i \le r-1 \tag{11}$$

However, the conditions of output decoupling from disturbance are very stringent and generally only hold in very special cases.

B. Details of Proposed UDE-FLSMC Method

When the output decoupling from disturbance cannot be achieved, a UDE-FLSMC method is proposed in this paper to improve the anti-disturbance capability of the system. By letting $\boldsymbol{A}\boldsymbol{z} = \boldsymbol{f}_{vo}(z)$ and $\boldsymbol{B}\boldsymbol{v} = b_2\boldsymbol{u}$ in the first term of (10), while decomposing $\boldsymbol{q}(z)$ in the second term into internal and external variable forms $\boldsymbol{q}(z) = \boldsymbol{f}_{vi}(z) + b_1 z_{vo}$, (10) can be reorganized into the following form as:

$$\begin{cases} \dot{z}_{vo} = \boldsymbol{f}_{vo}(z) + b_2\boldsymbol{u} + \boldsymbol{w}_2(z) \\ \dot{z}_{vi} = \boldsymbol{f}_{vi}(z) + b_1 z_{vo} + \boldsymbol{w}_1(z) \\ \boldsymbol{y} = z(t) \end{cases} \tag{12}$$

where $\boldsymbol{f}_{vi}(z)$ and $\boldsymbol{f}_{vo}(z)$ are the known system model expressions; and b_1 and b_2 are the known coefficients. $\boldsymbol{w}_1(z)$ and the control input are not in the same channel, so $\boldsymbol{w}_1(z)$ is called unmatched disturbance; and $\boldsymbol{w}_2(z)$ and the control input are in the same channel, so $\boldsymbol{w}_2(z)$ is called matched disturbance.

The concepts of internal disturbance, external disturbance, lumped disturbance, unmatched disturbance, and matched disturbance can be illustrated with Fig. 1.

As shown in Fig. 1, $\boldsymbol{p}(\boldsymbol{x})\boldsymbol{w} = \Delta\boldsymbol{f}(\boldsymbol{x}) + \Delta\boldsymbol{g}(\boldsymbol{x})\boldsymbol{u} + \boldsymbol{d}(\boldsymbol{x})\boldsymbol{w}$ includes the system model uncertainties and dynamic disturbances, which represents the lumped disturbances. After feedback linearization, $\dot{z}_{vo} = \boldsymbol{A}\boldsymbol{z} + \boldsymbol{B}\boldsymbol{v} + \boldsymbol{c}(z)\boldsymbol{w}_2(z)$ is the external dynamics model; and $\dot{z}_{vi} = \boldsymbol{q}(z) + \boldsymbol{k}(z)\boldsymbol{w}_1(z)$ is the internal dynamics model. Then, by the variable substitution, $\boldsymbol{w}_2(z)$ is in the same channel with the control input $\boldsymbol{u}$ in $\dot{z}_{vo} = \boldsymbol{f}_{vo}(z) + \boldsymbol{b}_2\boldsymbol{u} + \boldsymbol{w}_2(z)$ and is the matched disturbance; $\boldsymbol{w}_1(z)$ is in the same channel with the input $\boldsymbol{u}$ and is the unmatched disturbance.

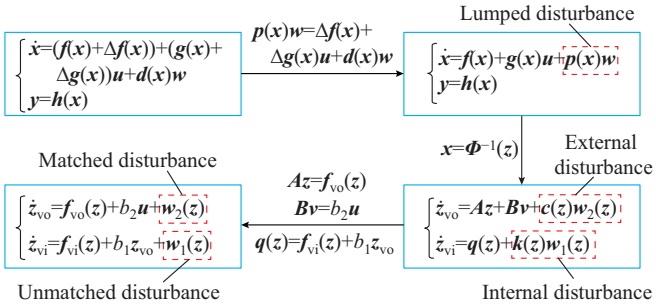

Fig. 1. Illustration of disturbances.

The control objective is to track the reference signal through a robust control law without being affected by lumped disturbances. The reference model is expressed as:

$$\begin{cases} \dot{z}_{vim} = \boldsymbol{f}_{vi}(z_m) + b_1 z_{vom} \\ \dot{z}_{vom} = \boldsymbol{f}_{vo}(z_m) + b_2\boldsymbol{u}_m \\ \boldsymbol{y}_m = \boldsymbol{z}_m \end{cases} \tag{13}$$

where z_{vom} and z_{vim} are the external and internal states of the reference model, respectively; $\boldsymbol{u}_m$ is the control input of the reference model; $\boldsymbol{y}_m$ is the output of the reference model; and z_m is the system state of the reference model.

The tracking error of the system model to the reference model is defined as:

$$\begin{cases} \boldsymbol{e}_{vi} = z_{vim} - z_{vi} \\ \boldsymbol{e}_{vo} = \dot{\boldsymbol{e}}_{vi} + \boldsymbol{w}_1(z) = \boldsymbol{f}_{vo}(\boldsymbol{e}_{vi}) + b_1(z_{vom} - z_{vo}) \end{cases} \tag{14}$$

where $\boldsymbol{e}_{vi}$ is the internal system tracking error; and $\boldsymbol{e}_{vo}$ is the external system tracking error.

The derivations for $\boldsymbol{e}_{vi}$ and $\boldsymbol{e}_{vo}$ are obtained as:

$$\begin{cases} \dot{\boldsymbol{e}}_{vi} = \boldsymbol{e}_{vo} - \boldsymbol{w}_1(z) \\ \dot{\boldsymbol{e}}_{vo} = \dot{\boldsymbol{f}}_{vo}(\boldsymbol{e}_{vi}) + b_1(\boldsymbol{f}_{vo}(z_m) + b_2\boldsymbol{u}_m) - b_1(\boldsymbol{f}_{vo}(z) + b_2\boldsymbol{u}) - \boldsymbol{w}_2(z) \end{cases} \tag{15}$$

In order to achieve zero tracking error, the following sliding mode surface $\boldsymbol{\sigma}$ is constructed as:

$$\boldsymbol{\sigma} = c_1\boldsymbol{e}_{vi} + c_2\boldsymbol{e}_{vo} \tag{16}$$

where $c_1 > 0$ and $c_2 > 0$ are the positive coefficients.

Combining with (15) and taking the derivative of the sliding surface, we can obtain:

$$\dot{\boldsymbol{\sigma}} = c_1\boldsymbol{e}_{vo} + c_2\dot{\boldsymbol{f}}_{vo}(\boldsymbol{e}_{vi}) + c_2 b_1(\boldsymbol{f}_{vo}(z_m) + b_2\boldsymbol{u}_m) - c_2 b_1(\boldsymbol{f}_{vo}(z) + b_2\boldsymbol{u}) + \boldsymbol{u}_{de} \tag{17}$$

where $\boldsymbol{u}_{de} = -c_1\boldsymbol{w}_1(z) - c_2 b_1\boldsymbol{w}_2(z)$ is the lumped disturbance.

Choosing the sliding mode reaching law as $\dot{\boldsymbol{\sigma}} = -n\boldsymbol{\sigma}$ and replacing the disturbance $\boldsymbol{u}_{de}$ with the estimated value $\hat{\boldsymbol{u}}_{de}$, we

can obtain the control input $\boldsymbol{u}$ as:

$$\boldsymbol{u}=\boldsymbol{u}_{\mathrm{m}}+\frac{1}{b_2}\left(\boldsymbol{f}_{\mathrm{vo}}\left(\boldsymbol{z}_{\mathrm{m}}\right)-\boldsymbol{f}_{\mathrm{vo}}\left(\boldsymbol{z}\right)\right)+\frac{1}{c_2b_1b_2}\left(c_1\boldsymbol{e}_{\mathrm{vo}}+c_2\dot{\boldsymbol{f}}_{\mathrm{vo}}\left(\boldsymbol{e}_{\mathrm{vi}}\right)+n\boldsymbol{\sigma}+\hat{\boldsymbol{u}}_{\mathrm{de}}\right) \tag{18}$$

where $n>0$ is a positive coefficient; and $\hat{\boldsymbol{u}}_{\mathrm{de}}$ includes both matched and unmatched disturbances. Therefore, the proposed UDE-FLSMC method can handle both matched and unmatched disturbances.

Then, substituting $\boldsymbol{u}$ in (18) into (17), we have:

$$\dot{\boldsymbol{\sigma}}=c_1\boldsymbol{e}_{\mathrm{vo}}+c_2\dot{\boldsymbol{f}}_{\mathrm{vo}}\left(\boldsymbol{e}_{\mathrm{vi}}\right)+c_2b_1\boldsymbol{f}_{\mathrm{vo}}\left(\boldsymbol{z}_{\mathrm{m}}\right)+c_2b_1b_2\boldsymbol{u}_{\mathrm{m}}-c_2b_1\boldsymbol{f}_{\mathrm{vo}}\left(\boldsymbol{z}\right)+\boldsymbol{u}_{\mathrm{de}}-c_2b_1b_2\boldsymbol{u}_{\mathrm{m}}-c_2b_1\boldsymbol{f}_{\mathrm{vo}}\left(\boldsymbol{z}_{\mathrm{m}}\right)+c_2b_1\boldsymbol{f}_{\mathrm{vo}}\left(\boldsymbol{z}\right)-c_1\boldsymbol{e}_{\mathrm{vo}}-c_2\dot{\boldsymbol{f}}_{\mathrm{vo}}\left(\boldsymbol{e}_{\mathrm{vi}}\right)-n\boldsymbol{\sigma}-\hat{\boldsymbol{u}}_{\mathrm{de}} \tag{19}$$

Eliminating similar terms, we can obtain:

$$\boldsymbol{u}_{\mathrm{de}}=\dot{\boldsymbol{\sigma}}+\hat{\boldsymbol{u}}_{\mathrm{de}}+n\boldsymbol{\sigma} \tag{20}$$

Since the lumped disturbance contains the sliding surface derivative $\dot{\boldsymbol{\sigma}}$, which cannot be calculated directly, it can be estimated through a low-pass filter $G_f(s)$ as:

$$\hat{\boldsymbol{u}}_{\mathrm{de}}=\left(\dot{\boldsymbol{\sigma}}+\hat{\boldsymbol{u}}_{\mathrm{de}}+n\boldsymbol{\sigma}\right)*\mathcal{L}^{-1}\left\{G_f(s)\right\} \tag{21}$$

where $\mathcal{L}^{-1}$ is the Laplace inverse transform; * denotes the convolution operation; and $G_f(s)=(1/Ts+1)$ is the low-pass filter, and T is the time constant.

The Laplace transform of $\dot{\boldsymbol{\sigma}}$ is $s\boldsymbol{\sigma}$. From (21), we can obtain:

$$\hat{\boldsymbol{u}}_{\mathrm{de}}=\mathcal{L}^{-1}\left\{\frac{G_f(s)}{1-G_f(s)}(s+n)\right\}*\boldsymbol{\sigma} \tag{22}$$

Combining (18) and (22), the controller can be obtained as:

$$\boldsymbol{u}=\boldsymbol{u}_{\mathrm{m}}+\frac{1}{b_2}\left(\boldsymbol{f}_{\mathrm{vo}}\left(\boldsymbol{z}_{\mathrm{m}}\right)-\boldsymbol{f}_{\mathrm{vo}}\left(\boldsymbol{z}\right)\right)+\frac{1}{c_2b_1b_2}\left(c_1\boldsymbol{e}_{\mathrm{vo}}+c_2\dot{\boldsymbol{f}}_{\mathrm{vo}}\left(\boldsymbol{e}_{\mathrm{vi}}\right)+n\boldsymbol{\sigma}+\mathcal{L}^{-1}\left\{\frac{G_f(s)(s+k)}{1-G_f(s)}\right\}*\boldsymbol{\sigma}\right) \tag{23}$$

The above process can be summarized as follows. First, the sliding surface is constructed by defining the tracking error between the actual model and the reference model. Then, we can obtain the control input containing the lumped disturbance. The lumped disturbance includes both matched and unmatched disturbances. Finally, we estimate the disturbance through UDE and obtain the UDE-FLSMC.

C. Stability Analysis Based on Lyapunov Theory

A normal operation system must have robustness in addition to stability. In this subsection, the stability of proposed UDE-FLSMC method is verified by Lyapunov theory.

The Lyapunov function is constructed as:

$$V=\frac{1}{2}\boldsymbol{\sigma}^2 \tag{24}$$

The derivative of (24) is given as:

$$\dot{V}=\boldsymbol{\sigma}\dot{\boldsymbol{\sigma}}=-n\boldsymbol{\sigma}^2+\tilde{\boldsymbol{u}}_{\mathrm{de}}\boldsymbol{\sigma} \tag{25}$$

where $\tilde{\boldsymbol{u}}_{\mathrm{de}}=\boldsymbol{u}_{\mathrm{de}}-\hat{\boldsymbol{u}}_{\mathrm{de}}$ is the lumped disturbance estimation error.

As the disturbance is bounded, the estimation error is also bounded, denoted by $\boldsymbol{\rho}$ as:

$$\tilde{\boldsymbol{u}}_{\mathrm{de}}\le\boldsymbol{\rho} \tag{26}$$

Using Young's inequality combined with (25) and (26) yields:

$$\dot{V}\le-n\boldsymbol{\sigma}^2+\boldsymbol{\rho}\boldsymbol{\sigma}\le-n\boldsymbol{\sigma}^2+\frac{\boldsymbol{\sigma}^2}{2}+\frac{\boldsymbol{\rho}^2}{2}=-(2n-1)V+\frac{\boldsymbol{\rho}^2}{2} \tag{27}$$

Further solving the above equation yields:

$$0\le V(t)\le V(0)\mathrm{e}^{(1-2n)t}+\frac{\boldsymbol{\rho}^2}{2(2n-1)}\left(1-\mathrm{e}^{-(2n-1)t}\right) \tag{28}$$

If $n>0.5$ is chosen and the filter is well designed, the estimation error will be small, and the sliding mode surface is bounded. Therefore, the system is boundedly stable.

The control structure is shown in Fig. 2. The sliding mode surface designed based on the UDE eliminates the discontinuous switching terms in traditional sliding mode control, thereby avoiding the chattering problem. The designed control law exhibits strong robustness against both matched and unmatched disturbances. By applying the proposed UDE-FLSMC method to design the control structure for the grid-side converter of wind turbines, it will effectively suppress oscillation problems. Meanwhile, it only requires the design of a low-pass filtering time constant and three parameters related to the sliding mode surface.

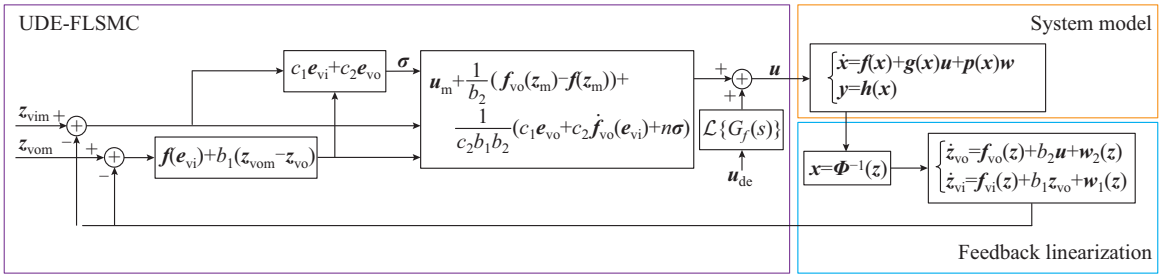

Fig. 2. Control structure.

III. Application of Proposed UDE-FLSMC Method in Wind Power Integrated System

In this section, the control structure of the wind power integrated system will be designed based on the proposed UDE-FLSMC method, and then the impedance model will be further developed to analyze the influence of control parameters on the impedance characteristics.

A. System Description

The structure of PMSGs integrated into an AC power grid is shown in Fig. 3, where L_{g1}-L_{g3} are different line inductors.

The wind farm consists of 100 sets of 1 MW PMSGs of the same model, with identical control parameters and operating conditions, and the root mean square (RMS) line voltage at the outlet of wind turbine is 0.69 kV. The wind turbines are connected to the 35 kV collector line through the box-type transformer at the end of the wind turbines (690 V/35 kV), and then to the 110 kV transmission line through a step-up transformer (35 kV/110 kV) at the outlet of wind farm. They are further connected to 220 kV transmission line via secondary step-up transformer (110 kV/220 kV), and finally connected to the 750 kV AC main grid by tertiary step-up transformer (220 kV/750 kV). All PMSGs in the wind farm can be equivalent to one wind turbine.

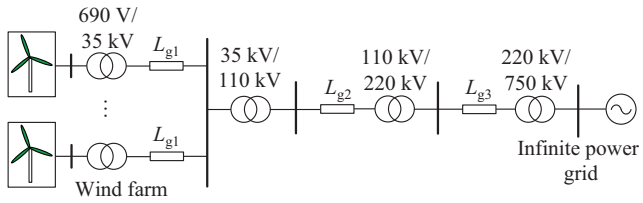

Fig. 3. Structure of PMSGs integrated into an AC power grid.

When the wind power integrated system operates stably, due to the blocking effect of DC capacitor between the machine-side converter (MSC) and the grid-side converter, the wind turbine, generator, and MSC can be simplified as a controlled current source model. And the change of the wind turbine output power can be simulated by adjusting the DC current. At the same time, the line and transformer impedance equivalences are normalized to the 0.69 kV side, then the wind power integrated system can be simplified into the converter integrated system, as shown in Fig. 4. The DC input of the converter is equivalent to a DC current source. In Fig. 4, e_a, e_b, and e_c are the output port voltages of the converter in abc coordinates; v_a, v_b, and v_c are the voltages at the grid connection point in abc coordinates; i_a, i_b, and i_c are the converter inductor currents in abc coordinates; v_{dc} is the DC voltage; L is the filter inductor; C is the DC capacitance; $H_{PLL}(s)$ is the PLL transfer function; θ_{PLL} is the PLL angle, which provides the reference phase angle for Park transformation; and L_g is the line inductor. The three-phase grid voltages and currents in abc coordinates are transformed to dq coordinates using Park transformation, so e_d, e_q, v_d, v_q, i_d, and i_q are the corresponding variables in the dq coordinates.

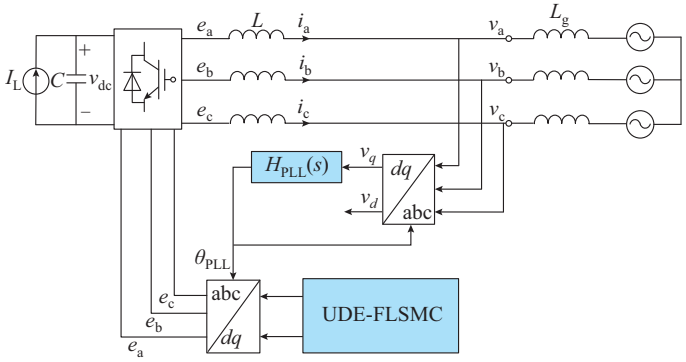

Fig. 4. Converter integrated system.

The dynamic mathematical model of the converter is given as:

$$\begin{cases} \dfrac{\mathrm{d}i_d}{\mathrm{d}t} = \dfrac{e_d}{L} - \dfrac{v_d}{L} + \omega i_q \\ \dfrac{\mathrm{d}i_q}{\mathrm{d}t} = \dfrac{e_q}{L} - \dfrac{v_q}{L} - \omega i_d \\ \dfrac{\mathrm{d}\Delta\theta_{\mathrm{PLL}}}{\mathrm{d}t} = k_{\mathrm{i}} x_{\mathrm{PLL}} + k_{\mathrm{p}} v_q \\ \dfrac{\mathrm{d}v_{\mathrm{dc}}}{\mathrm{d}t} = \dfrac{i_{\mathrm{dc}}}{C} - \dfrac{3i_d e_d}{2CV_{\mathrm{dc}}} - \dfrac{3i_q e_q}{2CV_{\mathrm{dc}}} \end{cases} \tag{29}$$

where ω is the angular frequency; $\Delta\theta_{PLL}$ is the variation of PLL; x_{PLL} is the intermediate variable of the PLL; and k_p and k_i are the proportional and integral coefficients of the PLL, respectively.

B. Control Design of Grid-side Converters

1) Feedback Linearization

First, the feedback linearization of (29) is performed by choosing the state variables $\boldsymbol{x} = [x_1, x_2] = [i_d, i_q]$, the control variables $\boldsymbol{u} = [u_1, u_2] = [e_d, e_q]$, and the output variables $\boldsymbol{h} = [h_1, h_2] = [i_d, i_q]$. Then, organizing (29) into the affine nonlinear system form yields:

$$\boldsymbol{f}(\boldsymbol{x}) = \begin{bmatrix} \omega x_2 \\ \omega x_1 \\ k_{\mathrm{p}} u_q \\ \dfrac{i_{\mathrm{dc}}}{C} \end{bmatrix} \boldsymbol{g}(\boldsymbol{x}) = \begin{bmatrix} \dfrac{1}{L} & 0 \\ 0 & \dfrac{1}{L} \\ 0 & 0 \\ \dfrac{-3i_d}{2CU_{\mathrm{dc}}} & \dfrac{-3i_q}{2CU_{\mathrm{dc}}} \end{bmatrix} \boldsymbol{p}(\boldsymbol{x}) = \begin{bmatrix} -\dfrac{u_d}{L} \\ -\dfrac{u_q}{L} \\ k_{\mathrm{i}} x_{\mathrm{PLL}} \\ 0 \end{bmatrix} \tag{30}$$

According to the definition of relative degree of the MIMO system, we have:

$$\begin{cases} L_{g_1} L_f^0 h_1(\boldsymbol{x}) = 1/L \\ L_{g_2} L_f^0 h_1(\boldsymbol{x}) = 0 \\ L_{g_1} L_f^0 h_2(\boldsymbol{x}) = 0 \\ L_{g_2} L_f^0 h_2(\boldsymbol{x}) = 1/L \end{cases} \tag{31}$$

Since the matrix $\boldsymbol{B}$ is non-singular, the total relative degree of each output of the system is $r = 1 + 1 = 2$. The relative degree is less than the system dimension, so partial feedback linearization can be achieved.

The external state variables of the system are i_d and i_q, the internal state variables are v_{dc} and $\Delta\theta_{PLL}$, and the coordinate transformation can be selected as:

$$\boldsymbol{\Phi}(\boldsymbol{x}) = \begin{bmatrix} z_1 \\ z_2 \\ z_3 \\ z_4 \end{bmatrix} = \begin{bmatrix} h_1 \\ h_2 \\ \varphi_3 \\ \varphi_4 \end{bmatrix} = \begin{bmatrix} i_d \\ i_q \\ v_{\mathrm{dc}} \\ \Delta\theta_{\mathrm{PLL}} \end{bmatrix} \tag{32}$$

The Jacobian matrix obtained by (32) is given as:

$$\boldsymbol{J}_{\boldsymbol{\Phi}} = \partial\boldsymbol{\Phi}(\boldsymbol{x})/\partial\boldsymbol{x} \neq \boldsymbol{0} \tag{33}$$

Therefore, the chosen coordinate transformation is qualified.

The system equation after feedback linearization is given as:

$$\begin{cases} \dot{z}_1 = \omega z_2 + u_1/L - v_d/L \\ \dot{z}_2 = -\omega z_1 + u_2/L - v_q/L \\ \dot{z}_3 = -3z_1u_1/\left(2CV_{\mathrm{dc}}\right) - 3z_2u_2/\left(2CV_{\mathrm{dc}}\right) + i_{\mathrm{dc}}/C \\ \dot{z}_4 = k_{\mathrm{i}}x_{\mathrm{PLL}} + k_{\mathrm{p}}v_q \end{cases} \tag{34}$$

Then, the disturbance decoupling condition is expressed as:

$$\begin{cases} L_pL_f^{1-1}h_1(\boldsymbol{x}) = L_ph_1(\boldsymbol{x}) = -1/L \\ L_pL_f^{1-1}h_2(\boldsymbol{x}) = L_ph_2(\boldsymbol{x}) = -1/L \end{cases} \tag{35}$$

By combining (11) and (35), it can be observed that the system model cannot achieve disturbance decoupling after feedback linearization.

2) UDE-based Sliding Mode Control

With the variable substitutions $z_{\mathrm{vo1}}=z_1$, $z_{\mathrm{vo2}}=z_2$, $z_{\mathrm{vi1}}=z_3$, and $z_{\mathrm{vi2}}=z_4$, (34) is reorganized and expressed as:

$$\begin{cases} \begin{bmatrix} \dot{z}_{\mathrm{vi1}} \\ \dot{z}_{\mathrm{vi2}} \end{bmatrix} = \begin{bmatrix} 0 \\ k_{\mathrm{p}}v_q \end{bmatrix} + \begin{bmatrix} \dfrac{-3e_d}{2CV_{\mathrm{dc}}} & \dfrac{-3e_q}{2CV_{\mathrm{dc}}} \\ 0 & 1 \end{bmatrix} \begin{bmatrix} z_{\mathrm{vi1}} \\ z_{\mathrm{vi2}} \end{bmatrix} + \begin{bmatrix} \dfrac{i_{\mathrm{dc}}}{C} \\ k_{\mathrm{i}}x_{\mathrm{PLL}} - i_q \end{bmatrix} \\ \begin{bmatrix} \dot{z}_{\mathrm{vo1}} \\ \dot{z}_{\mathrm{vo2}} \end{bmatrix} = \begin{bmatrix} -\dfrac{U_d}{L} + \omega z_{\mathrm{vo2}} \\ -\dfrac{U_q}{L} - \omega z_{\mathrm{vo1}} \end{bmatrix} + \begin{bmatrix} \dfrac{1}{L} & 0 \\ 0 & \dfrac{1}{L} \end{bmatrix} \begin{bmatrix} u_1 \\ u_2 \end{bmatrix} \end{cases} \tag{36}$$

Then, the tracking error is obtained as:

$$\begin{cases} \boldsymbol{e}_{\mathrm{vi}} = \begin{bmatrix} e_{\mathrm{vi1}} \\ e_{\mathrm{vi2}} \end{bmatrix} = \begin{bmatrix} z_{\mathrm{vi1,ref}} - z_{\mathrm{vi1}} \\ z_{\mathrm{vi2,ref}} - z_{\mathrm{vi2}} \end{bmatrix} \\ \boldsymbol{e}_{\mathrm{vo}} = \begin{bmatrix} e_{\mathrm{vo1}} \\ e_{\mathrm{vo2}} \end{bmatrix} = \begin{bmatrix} \dfrac{-3e_d}{2CU_{\mathrm{dc}}} & \dfrac{-3e_q}{2CU_{\mathrm{dc}}} \\ 0 & 1 \end{bmatrix} \begin{bmatrix} z_{\mathrm{vo1,ref}} - z_{\mathrm{vo1}} \\ z_{\mathrm{vo2,ref}} - z_{\mathrm{vo2}} \end{bmatrix} \end{cases} \tag{37}$$

where the subscript "ref" denotes the reference value of variable. By substituting (37) into (16), the sliding mode surface is given as:

$$\boldsymbol{\sigma} = c_1\boldsymbol{e}_{\mathrm{vi}} + c_2\boldsymbol{e}_{\mathrm{vo}} = \begin{bmatrix} c_1\left(z_{\mathrm{vi1,ref}} - z_{\mathrm{vi1}}\right) - c_2\dfrac{3e_d\left(z_{\mathrm{vo1,ref}} - z_{\mathrm{vo1}}\right) + 3e_q\left(z_{\mathrm{vo2,ref}} - z_{\mathrm{vo2}}\right)}{2CU_{\mathrm{dc}}} \\ c_1\left(z_{\mathrm{vi2,ref}} - z_{\mathrm{vi2}}\right) + c_2\left(z_{\mathrm{vo2,ref}} - z_{\mathrm{vo2}}\right) \end{bmatrix} \tag{38}$$

Then, $\hat{\boldsymbol{u}}_{\mathrm{de}}$ can be obtained as:

$$\hat{\boldsymbol{u}}_{\mathrm{de}} = \frac{s+n}{Ts}\boldsymbol{\sigma} \tag{39}$$

By substituting (37)-(39) into (23), the final designed controller is expressed as:

$$\boldsymbol{u}_{\mathrm{m}} = \begin{bmatrix} e_d \\ e_q \end{bmatrix} = \begin{bmatrix} v_{d,\mathrm{ref}} \\ v_{q,\mathrm{ref}} \end{bmatrix} + \frac{1}{b_2}\begin{bmatrix} \dfrac{-v_{d,\mathrm{ref}}}{L} + \omega i_{q,\mathrm{ref}} + \dfrac{v_d}{L} - \omega i_q \\ \dfrac{-v_{q,\mathrm{ref}}}{L} - \omega i_{d,\mathrm{ref}} + \dfrac{v_q}{L} + \omega i_d \end{bmatrix} + \frac{1}{c_2b_1b_2}\left(c_1\boldsymbol{e}_{\mathrm{vo}} + c_2\dot{f}_{\mathrm{vo}}\left(\boldsymbol{e}_{\mathrm{vi}}\right) + n\boldsymbol{\sigma}\right) + \frac{1}{c_2b_1b_2}\frac{s+n}{Ts}\boldsymbol{\sigma} \tag{40}$$

The control structure of PMSG obtained from the design of (40) will be more adaptable to system disturbances and uncertainties. In order to analyze the ability of the proposed UDE-FLSMC method to suppress oscillations, the impedance model needs to be further developed.

IV. Impedance Characteristic Analysis and Stability Analysis of Wind Power Integrated System

The impedance-based stability analysis method can intuitively reflect the full frequency band characteristics and has become an effective method for small disturbance stability analysis. In this section, the impedance model of the proposed UDE-FLSMC method is developed and its impedance characteristics and stability under weak grid conditions are analyzed.

A. Impedance Characteristic Analysis

Based on the harmonic linearization, this subsection derives the transmission process of disturbance component in the control sector and establishes the frequency coupled impedance model of the converter [30], which can be represented by the following two-dimensional matrix:

$$\begin{bmatrix} Y_{11}(s) & Y_{12}(s) \\ Y_{21}(s) & Y_{22}(s) \end{bmatrix} = \begin{bmatrix} C_{11} - N_{11} & C_{12} - N_{12} \\ C_{21} - N_{21} & C_{22} - N_{22} \end{bmatrix}^{-1} \cdot \begin{bmatrix} 1 - G_{11} - M_{11} & -G_{12} - M_{12} \\ -G_{21} - M_{21} & 1 - G_{22} - M_{22} \end{bmatrix} \tag{41}$$

where $Y_{ij}(s)$ is the admittance of converter; and C_{ij}, N_{ij}, G_{ij}, and M_{ij} are the elements of admittance, and their expressions are given in Supplementary Material A. Considering the grid impedance, the effect of negative-sequence coupling term can be equivalent to that of the positive-sequence coupling term as:

$$Y_{\mathrm{p}} = \frac{I_{\mathrm{p}}\left[f_{\mathrm{p}}\right]}{V_{\mathrm{p}}\left[f_{\mathrm{p}}\right]} = Y_{11}(s) - \frac{Y_{12}(s)Z_{\mathrm{g}}\left(s - \mathrm{j}2\omega_1\right)Y_{21}(s)}{1 + Y_{22}(s)Z_{\mathrm{g}}\left(s - \mathrm{j}2\omega_1\right)} \tag{42}$$

$$Z_{\mathrm{p}} = 1/Y_{\mathrm{p}} \tag{43}$$

where f_{p} is the positive-sequence disturbance frequency; V_{p} is the disturbance voltage; I_{p} is the disturbance current; ω_1 is the system angular frequency; Z_{g} is the grid impedance; and Y_{p} is the positive-sequence impedance.

The system parameters of Fig. 4 are shown in Table I.

TABLE I
System Parameters

Parameter	Symbol	Value
Rated RMS line voltage (V)	V_1	690
Rated active power (MW)	P_1	1
Frequency (Hz)	f_1	50
DC reference voltage (V)	V_{dc}	1200
DC capacitance (mF)	C	7
Filter inductor (mH)	L	1
Proportional coefficient of PLL	k_{p}	14.25
Integral coefficient of PLL	k_{i}	2862

B. Control Parameter Design and Impedance Characteristic Analysis

In the proposed UDE-FLSMC method, four control parameters need to be designed: the time constant of the low-pass filter T, and the parameters of the sliding mode surface n, c_1, and c_2. In the following text, the effect of different control parameters on impedance characteristics will be analyzed in order to select the appropriate control parameters.

The impedance characteristics with different values of c_1 and c_2 are shown in Fig. 5. The black dashed lines in the phase-frequency characteristics are ±90°, which are the boundaries of positive/negative damping. The region outside the black dashed line indicates the negative damping region of the impedance phase. The parameter c_1 mainly affects the impedance characteristics within the PLL bandwidth. As c_1 increases, the impedance amplitude of the converter decreases, and the positive damping region of the impedance phase first increases and then decreases. In other frequency bands, the impedance characteristics are basically unchanged.

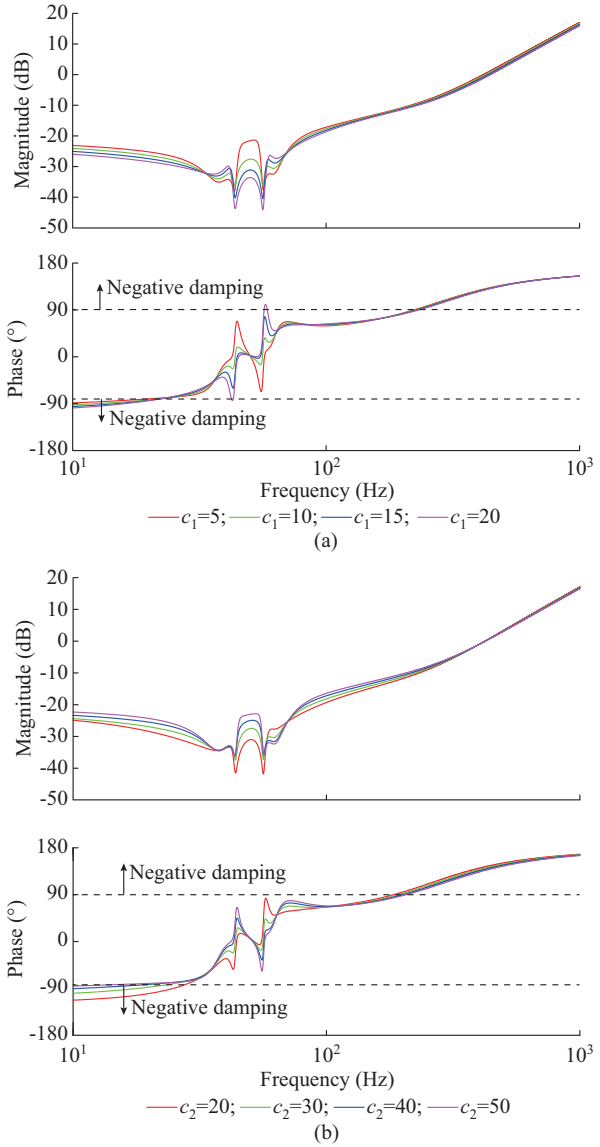

Fig. 5. Impedance characteristics with different values of c_1 and c_2. (a) With different values of c_1. (b) With different values of c_2.

The parameter c_2 also mainly affects the impedance characteristics within the PLL bandwidth. As c_2 increases, the impedance amplitude of the converter increases, and the positive damping region of the impedance phase decreases. In other frequency bands, the impedance characteristics are basically unchanged.

The impedance characteristics with different values of n and T are shown in Fig. 6. T has a significant impact on the impedance characteristics in super-synchronous and medium-to-high-frequency band. As T increases, the impedance magnitude decreases in super-synchronous band, the impedance magnitude increases in the medium-to-high-frequency band, and the impedance phases are closer to the negative damping region, which reduces the system stability in the medium-to-high-frequency band. The change of T has little effect on the impedance phase in the sub-synchronous band.

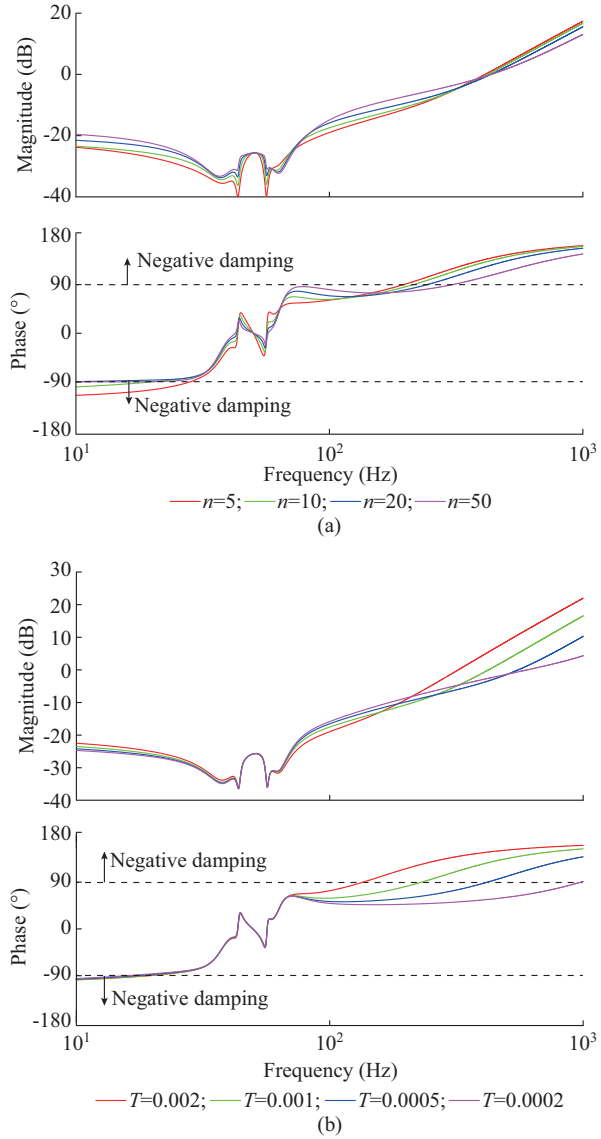

Fig. 6. Impedance characteristics with different values of n and T. (a) With different values of n. (b) With different values of T.

The parameter n also mainly affects the impedance characteristics in super-synchronous and medium-to-high-frequency band. As n increases, the impedance magnitude in super-syn-

chronous band increases, and the impedance phase also increases, tending to be closer to the negative damping region. In the medium-to-high-frequency band, the impedance magnitude decreases as n increase, while the impedance phase decreases, resulting in a larger positive damping region. The variation of n has little impact on the impedance phase in sub-synchronous frequency band.

The analytical results show that the time constant T and the parameter n have a significant effect on the stability characteristics of the wind turbine controller, while the effects of the parameters c_1 and c_2 are small and concentrated in PLL control band. Therefore, T and n are the crucial control parameters, and c_1 and c_2 only require satisfaction of the Hurwitz's stability conditions [31]. The sliding mode surface related parameters are selected as $c_1=8$ and $c_2=37$.

For the time constant T, the smaller T (the larger filter bandwidth), the stronger the anti-disturbance performance of UDE. However, the larger filter bandwidth, the greater influence of noise. Since the analysis mainly focuses on the frequency band below 100 Hz, T is chosen to be 0.001, and the filter bandwidth is 159.15 Hz. For the parameter n, the larger k is, the faster the sliding mode surface converges. In Fig. 6(a), the impedance phase tends to the negative damping region when k is larger, so k is chosen to be 10.

The designed control parameters can operate stably at different output power levels. In real engineering applications, when faced with transient stability problems, control switching or protection actions will be triggered. Whether the system can remain stable will depend on the transient control measures.

C. Stability Analysis

Currently, the grid-side converter usually adopts voltage-current double-closed-loop control, where the PI parameters of the voltage loop are taken as $k_p=0.32$, $k_i=40.53$, and the PI parameters of the current loop are taken as $k_p=0.56$, $k_i=530$, which are the same as those in Table I. In Fig. 3, the transformer and line impedances are normalized to the low-voltage side, and the total grid impedance is 0.028 mH (SCR is 1.1, indicating weak grid conditions). The stability analysis of the proposed UDE-FLSMC method is shown in Fig. 7. In Fig. 7, the black line in the magnitude-frequency characteristics is the magnitude of grid impedance. The black dashed lines in the phase-frequency characteristics are ±90°, which are the boundaries of positive and negative damping, and +90° is also the phase of the grid impedance. At the intersection of the converter and grid impedance amplitudes, if the converter impedance phase is in the negative damping region, there is a risk of oscillation.

From Fig. 7, it can be observed that the proposed UDE-FLSMC method has a larger positive damping region for the impedance phase compared with the PI control. The converter impedance with PI control intersects with the grid impedance at 55 Hz. At this point, the impedance phase is located in negative damping region, and there is a risk of oscillation. The converter impedance of the proposed UDE-FLSMC method intersects with the grid impedance at 55 Hz, while the impedance phase is still located in the positive damping region without the risk of oscillation. Therefore, the proposed UDE-FLSMC method can effectively suppress the system oscillation under weak grid conditions.

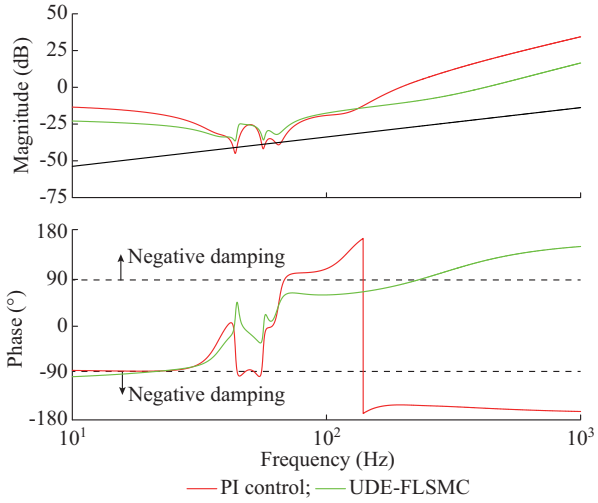

Fig. 7. Stability analysis of proposed UDE-FLSMC method.

V. Hardware-in-loop Experimental Verification

The actual power system contains large random noise and complex sampled signal components, which usually makes it difficult to realize the ideal performance of the controller. In order to verify the field application capability of proposed UDE-FLSMC method, the hardware-in-loop experiments are carried out using RTDS, and hardware controller is C-RIO 9039 of National Instruments (NI). The C-RIO is a high-performance embedded controller, which mainly consists of a real-time (RT) module, a field programmable gate array (FPGA) module, and an industrial-grade input/output (I/O) module. It is suitable for complex scenarios requiring high-speed processing and high reliability, such as distributed measurement systems and real-time control applications. The hardware-in-loop experimental platform based on RTDS and C-RIO 9039 is shown in Fig. 8.

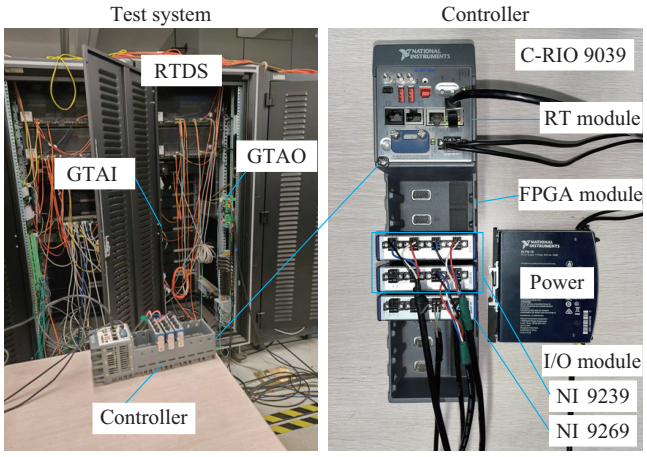

Fig. 8. Hardware-in-loop experimental platform.

The power grid and converter switching circuit are built in RTDS and the converter control structure is built in C-RIO 9039. The RTDS simulation model generates analog sig-

nals and outputs to C-RIO 9039 through the gigabit transceiver analytics output (GTAO) board. The controller obtains samples through the NI 9239 sampling board, and then inputs them into the FPGA module for control calculation. The generated control signals are then feedback to RTDS through the NI 9269 output board.

Based on the constructed platform, the control effect of the proposed UDE-FLSMC method will be tested in two aspects: oscillation suppression capability and anti-disturbance capability. The proposed UDE-FLSMC method is then compared with PI control and phase margin frequency division compensation [16] (PM-FDC) control.

A. Oscillation Suppression Capability

This subsection will test the oscillation suppression capability of the proposed UDE-FLSMC method by triggering oscillations through reducing grid strength and increasing output power. The control parameters and operating conditions remain consistent with those described in Section III.

1) Dynamic Performance Under Reduced Grid Strength

The interactions between the wind farm and the power grid under reduced grid strength tend to cause the system oscillations. As analyzed in Section III, the proposed UDE-FLSMC method better adapts to weak grid conditions than the PI control.

The transformer and line impedances in Fig. 3 are normalized to the low-voltage side, and the grid impedance is increased from 0.005 mH to 0.028 mH (SCR is reduced from 6.06 to 1.1) in 5.5 s. As shown in Fig. 9, the proposed UDE-FLSMC method and the PM-FDC control can both suppress oscillation when the grid strength is reduced, and the proposed UDE-FLSMC method has a better suppression effect. In contrast, PI control causes continuous oscillation and capacitor voltage instability.

2) Dynamic Performance Under Increased Output Power

The output power of the wind farm increases from 20 MW to 60 MW in 5.5 s, and the grid impedance is 0.01 mH (SCR is 3.03). As shown in Fig. 10, the proposed UDE-FLSMC method quickly restores stable operation. However, both the PI control and the PM-FDC control fail to maintain stable capacitor voltage, and the *d*-axis current reaches its limit, resulting in significant oscillation.

B. Anti-disturbance Capability

The proposed UDE-FLSMC method can not only suppress oscillations, but also improve the dynamic response characteristics of the system. Next, the anti-disturbance capability of the proposed UDE-FLSMC method will be tested in three aspects: AC voltage disturbances, system parameter uncertainties, and three-phase short-circuit faults.

1) Dynamic Performance Under AC Voltage Disturbance

The rated RMS line voltage of the wind turbine is 0.69 kV, and the corresponding phase voltage magnitude is 0.56 kV. At 5.5 s, it is assumed that the AC grid phase voltage steps from 0.56 kV to 0.50 kV.

As shown in Fig. 11, the converter based on PI control fails to maintain the stability of the DC capacitor voltage, and the *d*-axis current has reached the limit; for the converter based on the PM-FDC control, the capacitor voltage and *d*-axis current can restore stable operation after a longer period of regulation. In contrast, the proposed UDE-FLSMC method can quickly restore stable operation after disturbance, demonstrating strong anti-disturbance capability.

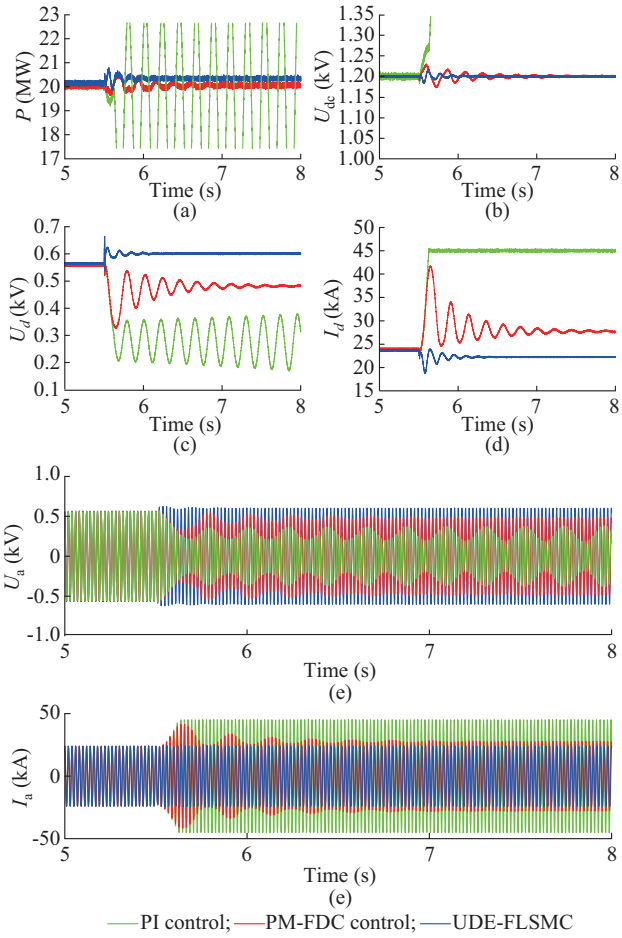

Fig. 9. Dynamic performance under reduced grid strength. (a) Power. (b) DC voltage. (c) *d*-axis voltage. (d) *d*-axis current. (e) a-phase voltage. (f) a-phase current.

2) Dynamic Performance Under Parameter Uncertainties

The parameters of the filter inductance are included in the control structure. However, the measured value of filter circuit may deviate from the true value, thus affecting the system control performance. In order to evaluate the adaptability of the proposed UDE-FLSMC method to the parameter uncertainty, it is assumed that the filter inductance deviates from the real value by 100%. The dynamic response characteristics during the power step are shown in Fig. 12, which shows that all the three control methods adapt to the system parameter uncertainties, and the proposed UDE-FLSMC method has a smaller overshoot and shorter regulation time.

3) Dynamic Performance Under Three-phase Short-circuit Fault

At 5.5 s, assume that a three-phase short-circuit fault occurs at the converter grid-connection point, and lasts for 0.05 s.

From Fig. 13, it can be observed that after the fault is removed, the proposed UDE-FLSMC method recovers stable operation after about 0.5 s, the PM-FDC control needs about 0.7

s, and the PI control needs about 2 s. Due to the occurrence of a three-phase short-circuit fault, all control methods exhibit significant overshoot, but ultimately regain stable operation.

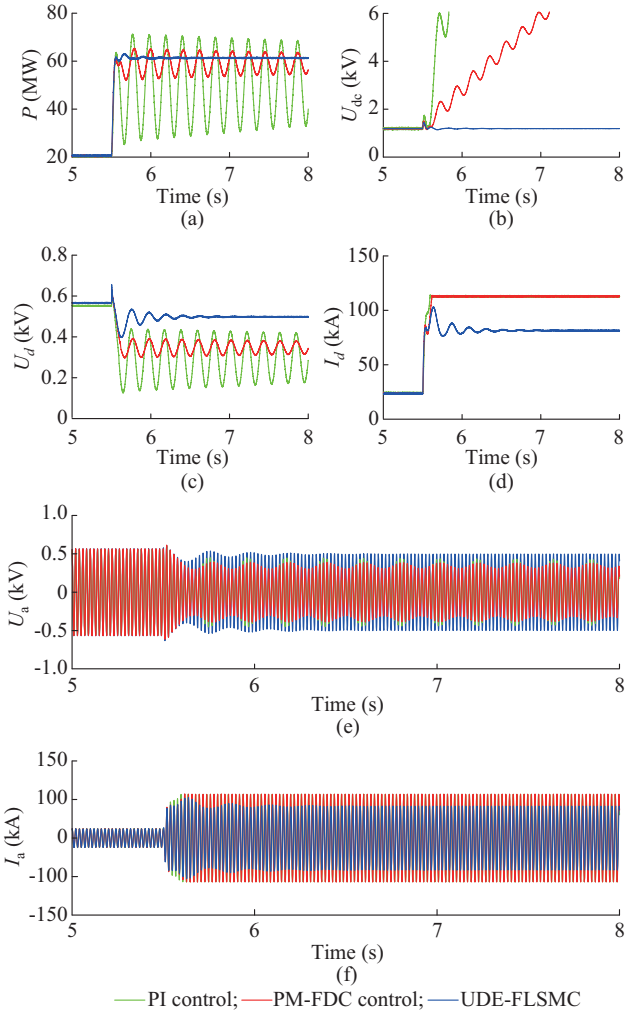

Fig. 10. Dynamic performance under increased output power. (a) Power. (b) DC voltage. (c) *d*-axis voltage. (d) *d*-axis current. (e) a-phase voltage. (f) a-phase current.

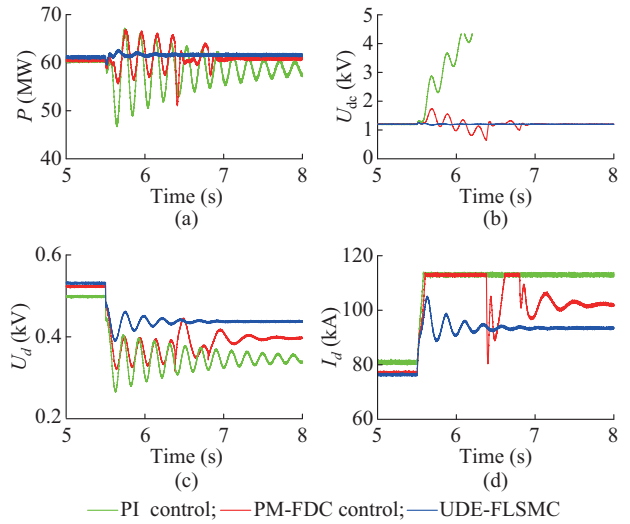

Fig. 11. Dynamic performance under AC voltage disturbance. (a) Power. (b) DC voltage. (c) *d*-axis voltage. (d) *d*-axis current.

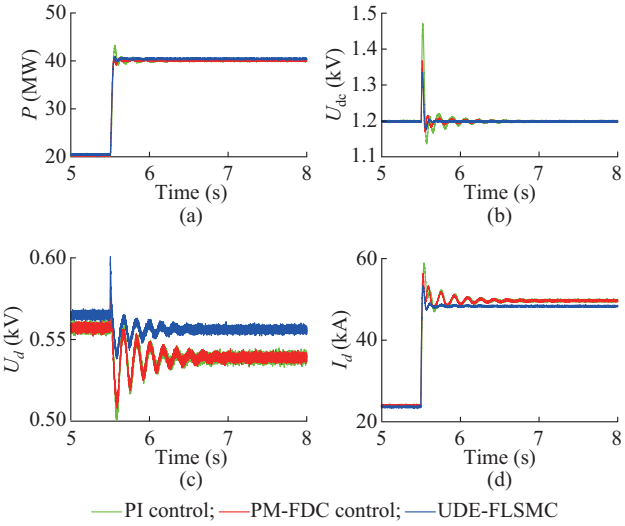

Fig. 12. Dynamic performance under parameter uncertainties. (a) Power. (b) DC voltage. (c) *d*-axis voltage. (d) *d*-axis current.

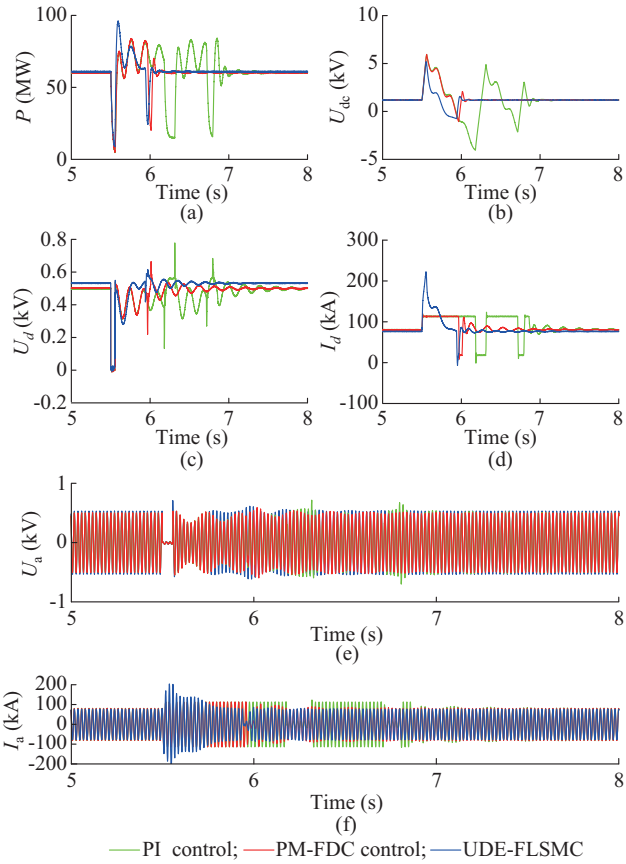

Fig. 13. Dynamic performance under three-phase short-circuit faults. (a) Power. (b) DC voltage. (c) *d*-axis voltage. (d) *d*-axis current. (e) a-phase voltage. (f) a-phase current.

C. Dynamic Response Characteristic Analysis

The experimental results show that the proposed UDE-FLSMC method has excellent dynamic performance compared with PI control. In order to analyze the dynamic response characteristics of PI control and the proposed UDE-FLSMC method, a transfer function model of the converter integrated system is established [32].

From [33], we can obtain the closed-loop transfer function model of the system between Δv_{dcr}^{*} and Δv_{dc} as:

$$\Delta v_{dc} = \frac{D(s)G_{dc}(s)}{D(s)G_{dc}(s) - sC_0V_{dcr}}\Delta v_{dcr}^{*} \tag{44}$$

where Δv_{dcr}^{*} is the reference value of DC voltage; and Δv_{dc} is the DC voltage variation. The denifitions of other varaibles can be referred to [33]. Then, we can obtain the frequency response characteristics of the closed-loop transfer functions of the PI control and the proposed UED-FLSMC method. As shown in Fig. 14, the bandwidth of the PI control is 62 Hz, and the bandwidth of the proposed UDE-FLSMC method is 78 Hz. When the bandwidth of the system is expanded by a factor of *N*, the response speed of the system is accelerated by a factor of *N*. Therefore, for the input signal, the larger the bandwidth, the stronger ability to track the control signal.

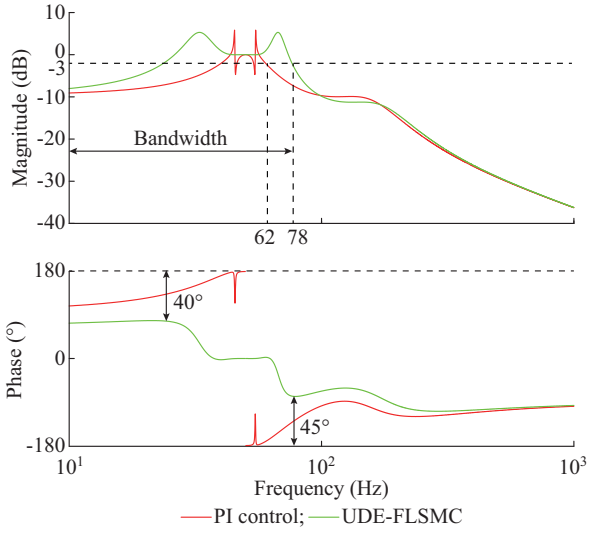

Fig. 14. Transfer function between Δv_{dcr}^{*} and Δv_{dc}.

At the same time, it can be observed from the phase-frequency characteristics that the PI control faces the risk of instability, while the proposed UDE-FLSMC method has a stability margin of more than 40°. The larger the phase margin, the stronger the system stability. Therefore, when subjected to disturbances, the proposed UDE-FLSMC method has stronger anti-disturbance ability and faster response characteristics than the PI control.

In this section, based on the hardware-in-loop experimental platform, the proposed UDE-FLSMC method is compared with the PI control and PM-FDC control in terms of oscillation suppression and anti-disturbance capabilities. The results show that the proposed UDE-FLSMC method has better dynamic performance and can significantly improve the system stability after disturbance. Then, the reasons for the excellent dynamic performance of the proposed UDE-FLSMC method are analyzed based on the transfer function model.

VI. Conclusion

To solve the oscillation problem of wind power integrated into the weak grid, this paper proposes a UDE-FLSMC method and designs the control structure of wind power integrated system. Then, the impedance model is established and the influence of the control parameter on stability is analyzed. Finally, the hardware-in-loop experiments are carried out based on RTDS and C-RIO platforms to verify the dynamic performance of wind power integrated system. The main conclusions are given as follows.

1) After feedback linearization, UDE is used to estimate the lumped disturbance in sliding mode control, which can not only eliminate the chattering problem, but also suppress both matched and unmatched disturbances. Then, the UDE-FLSMC method is proposed, which is effective in oscillation suppression.

2) The time constant of the low-pass filter *T* and the parameter of the sliding mode surface *n* are the crucial control parameters. The impedance characteristic analysis shows that there is still a large positive damping region in the impedance phase in the low-medium frequency bands when the control parameters are changed, so that the proposed UDE-FLSMC method has a stronger oscillation suppression capability.

3) Hardware-in-loop experiments show that, compared with the PI control and PM-FDC control, the proposed UDE-FLSMC method has not only stronger oscillation suppression ability, but also faster response speed and better regulation performance after disturbance.

References

[1] H. Gao, T. Jin, G. Wang *et al.*, "Low-carbon dispatching for virtual power plant with aggregated distributed energy storage considering spatiotemporal distribution of cleanness value," *Journal of Modern Power Systems and Clean Energy*, vol. 12, no. 2, pp. 346-358, Mar. 2024.

[2] Z. Zhang and C. Kang, "Challenges and prospects for constructing the new-type power system towards a carbon neutrality future," *Proceedings of the CSEE*, vol. 42, no. 2, pp. 2806-2819, Apr. 2022.

[3] L. Chen, S. Xu, H. Sun *et al.*, "A survey on wide-frequency oscillation for power systems with high penetration of power electronics," *Proceedings of the CSEE*, vol. 41, no. 7, pp. 2297-2310, Apr. 2021.

[4] L. Wang, X. Xie, Q. Jiang *et al.*, "Investigation of SSR in practical DFIG-based wind farms connected to a series-compensated power system," *IEEE Transactions on Power Systems*, vol. 30, no. 5, pp. 2772-2779, Nov. 2014.

[5] H. Liu, X. Xie, J. He *et al.*, "Subsynchronous interaction between direct-drive pmsg based wind farms and weak AC networks," *IEEE Transactions on Power Systems*, vol. 32, no. 6, pp. 4708-4720, Nov. 2017.

[6] B. Wen, D. Boroyevich, R. Burgos *et al.*, "Analysis of D-Q small-signal impedance of grid-tied inverters," *IEEE Transactions on Power Electronics*, vol. 31, no. 1, pp. 675-687, Jan. 2016.

[7] C. Zhang, W. Wang, G. He *et al.*, "Analysis of sub-synchronous oscillation of full-converter wind farm based on sequence impedance and an optimized design method for PLL parameters," *Proceedings of the CSEE*, vol. 37, no. 23, pp. 6757-6767, Dec. 2017.

[8] Y. Huang, X. Yuan, J. Hu *et al.*, "Modeling of VSC connected to weak grid for stability analysis of DC-link voltage control," *IEEE Journal of Emerging and Selected Topics in Power Electronics*, vol. 3, no. 4, pp. 1193-1204, Dec. 2015.

[9] G. Li, W. Wang, C. Liu *et al.*, "Mechanism analysis and suppression method of wideband oscillation of PMSG wind farms connected to weak grid (part I): analysis of wideband impedance characteristics and oscillation mechanism," *Proceedings of the CSEE*, vol. 39, no. 22, pp. 6547-6562, Nov. 2021.

[10] Y. Chen, X. Ruan, Z. Lin *et al.*, "A reconstructed singular return ratio matrix for optimizing design of the PLL in grid-connected inverters," *IEEE Transactions on Industrial Electronics*, vol. 70, no. 12, pp.

12453-12464, Dec. 2023.
[11] J. Xu, J. Zhong, J. Kang *et al*., "Stability analysis and robust parameter design of DC-Voltage Loop for three-phase grid-connected PV inverter under weak grid condition," *IEEE Transactions on Industrial Electronics*, vol. 71, no. 4, pp. 3776-3787, Apr. 2024.
[12] J. Lyu, X. Cai, and M. Molinas, "Optimal design of controller parameters for improving the stability of MMC-HVDC for wind farm integration," *IEEE Journal of Emerging and Selected Topics in Power Electronics*, vol. 6, no. 1, pp. 40-53, Mar. 2018.
[13] T. Huang, F. Yang, D. Zhang *et al*., "High-frequency stability analysis and impedance optimization for an MMC-HVDC integrated system considering delay effects," *IEEE Journal on Emerging and Selected Topics in Circuits and Systems*, vol. 12, no. 1, pp. 59-72, Mar. 2022.
[14] D. Zhang and X. Chen, "Overview of broadband oscillation mitigation of new energy generation power system based on impedance perspective," *Proceedings of the CSEE*, vol. 44, no. 24, pp. 9672-9691, Dec. 2024.
[15] G. Li, W. Wang, C. Liu *et al*., "Mechanism analysis and suppression method of wideband oscillation of PMSG wind farms connected to weak grid (part II): suppression method of wideband oscillation based on impedance reshaping," *Proceedings of the CSEE*, vol. 39, no. 23, pp. 6908-6920, Dec. 2019.
[16] X. Tang, Y. He, Z. Li *et al*., "Frequency division compensation method for phase margin of grid connected converters in the weak grid," *Proceedings of the CSEE*, vol. 44, no. 4, pp. 1565-1576, Feb. 2024.
[17] M. Yang, Z. Yang, Y. Li *et al*., "Impedance remodeling control strategy of grid-connected inverter based on feedforward voltage under weak grid," *Transactions of China Electrotechnical Society*, vol. 39, no. 8, pp. 2553-2566, Apr. 2024.
[18] B. Guo, X. Zhang, H. Ma *et al*., "A series impedance reshaping control method considering PLL dynamics for grid-connected inverters under weak grid conditions," *IEEE Transactions on Industrial Electronics*, vol. 71, no. 5, pp. 4896-4910, May 2024.
[19] J. Wang, W. Chen, Y. Liu *et al*., "High-frequency resonance analysis and impedance reshaping control of MMC-HVDC system based on frequency coupling impedance model," *Journal of Modern Power Systems and Clean Energy*, vol. 12, no. 2, pp. 646-657, Mar. 2024.
[20] C. Li, Y. Yang, Y. Cao *et al*., "Grid inertia and damping support enabled by proposed virtual inductance control for grid-forming virtual synchronous generator," *IEEE Transactions on Power Electronics*, vol. 38, no. 1, pp. 294-303, Jan. 2023.
[21] H. Yu, J. Lyu, X. Li *et al*., "Comprehensive evaluation of impact of high-frequency oscillation suppression strategy on the dynamic performance of flexible HVDC transmission system," *Proceedings of the CSEE*, vol. 42, no. 8, pp. 2873-2889, Apr. 2022.
[22] M. A. Chowdhury and G. M. Shafiullah, "SSR mitigation of series-compensated DFIG wind farms by a nonlinear damping controller using partial feedback linearization," *IEEE Transactions on Power Systems*, vol. 33, no. 3, pp. 2528-2538, May 2018.
[23] P. Li, J. Wang, and F. Wu, "Sub-synchronous control interaction mitigation for DFIGs by sliding mode control strategy based on feedback linearization," *Transactions of China Electrotechnical Society*, vol. 34, no. 17, pp. 3661-3671, Sept. 2019.
[24] H. Ding, J. Wang, X. Guo *et al.*, "Fixed-time sliding-mode disturbance observer-based finite-time backstepping control for current source rectifier," *IEEE Journal of Emerging and Selected Topics in Power Electronics*, vol. 12, no. 5, pp. 4767-4778, Oct. 2024.
[25] B. Shao, S. Zhao, Y. Yang *et al*., "Nonlinear subsynchronous oscillation damping controller for direct-drive wind farms with VSC-HVDC systems," *IEEE Journal of Emerging and Selected Topics in Power Electronics*, vol. 10, no. 3, pp. 2842-2858, Jun. 2022.
[26] B. Shao, S. Zhao, B. Gao *et al*., "Sub-synchronous oscillation mitigation strategy of direct-drive wind farms via VSC-HVDC system based on feedback linearization sliding mode control," *Proceedings of the CSEE*, vol. 41, no. 9, pp. 3090-3106, May. 2021.
[27] Y. Wang, B. Ren, and Q-C. Zhong, "Bounded UDE-based controller for input constrained systems with uncertainties and disturbances," *IEEE Transactions on Industrial Electronics*, vol. 68, no. 2, pp. 1560-1570, Feb. 2021.
[28] J. Chen, Y. Ren, Q. Meng *et al*., "Sub-synchronous oscillation suppression strategy for grid-forming direct-drive permanent magnet synchronous generator with uncertainty and disturbance estimator supplementary damping branch," *Transactions of China Electrotechnical Society*, vol. 39, no. 7, pp. 1985-2000, Apr. 2024.
[29] C. Fu, C. Zhang, G. Zhang *et al*., "Disturbance observer-based finite-time control for three-phase AC-DC converter," *IEEE Transactions on Industrial Electronics*, vol. 69, no. 6, pp. 5637-5647, Jun. 2022
[30] H. Nian, Y. Xu, L. Chen *et al*., "Frequency coupling characteristic modeling of grid-connected inverter and system stability analysis," *Proceedings of the CSEE*, vol. 39, no. 5, pp. 1421-1432, Mar. 2019.
[31] P. Li, W. Sun, W. Li *et al*., "Application of improved integral sliding surface to flight control system," *Control Engineering of China*, vol. 17, no. 3, pp. 269-271, May 2010.
[32] H. Yu, J. Lyu, X. Li *et al*., "Comprehensive evaluation of impact of high-frequency oscillation suppression strategy on the dynamic performance of flexible HVDC transmission system," *Proceedings of the CSEE*, vol. 42, no. 8, pp. 2873-2889, Apr. 2022.
[33] T. Wu, Q. Jiang, J. Shair *et al*., "Inclusion of current limiter nonlinearity in the characteristic analysis of sustained subsynchronous oscillations in grid-connected PMSGs," *IEEE Transactions on Energy Conversion*, vol. 36, no. 3, pp. 2416-2426, Sept. 2021.

Yanhui Xu received the Ph.D. degree in electrical engineering from North China Electric Power University, Beijing, China, in 2010. He is currently a Professor with North China Electric Power University. His research interests include dynamic power system analysis and load modeling.

Jiayan Li is currently pursuing the Ph.D. degree in electrical engineering at North China Electric Power University, Beijing, China. His research interests include renewable energy power system analysis and control.